The Astrophysical Journal, 922:207 (12pp), 2021 December 1 https://doi.org/10.3847/1538-4357/ac2a44

Probing Gas Kinematics and PDR Structure around O-type Stars in the Sh 2-305 H II Region

N. K. Bhadari[1,2], L. K. Dewangan[1], P. M. Zemlyanukha[3], D. K. Ojha[4], I. I. Zinchenko[3], and Saurabh Sharma[5]
[1] Physical Research Laboratory, Navrangpura, Ahmedabad 380009, India; naval@prl.res.in
[2] Indian Institute of Technology Gandhinagar Palaj, Gandhinagar 382355, India
[3] Institute of Applied Physics of the Russian Academy of Sciences 46 Ul′yanov str., 603950 Nizhny Novgorod, Russia
[4] Department of Astronomy and Astrophysics, Tata Institute of Fundamental Research, Homi Bhabha Road, Mumbai 400005, India
[5] Aryabhatta Research Institute of Observational Sciences, Manora Peak, Nainital 263002, India
Received 2021 June 7; revised 2021 September 10; accepted 2021 September 21; published 2021 December 1

Abstract

We report an observational study of the Galactic H II region Sh 2-305/S305 using the [C II] 158 μm line data, which are used to examine the gas dynamics and structure of photodissociation regions. The integrated [C II] emission map at [39.4, 49.5] km s^{-1} spatially traces two shell-like structures (i.e., inner and outer neutral shells) having a total mass of $\sim$565 $M_{\odot}$. The inner neutral shell encompasses an O9.5V star at its center and has a compact ring-like appearance. However, the outer shell is seen with more extended and diffuse [C II] emission, hosting an O8.5V star at its center, and surrounds the inner neutral shell. The velocity channel maps and position–velocity diagrams confirm the presence of a compact [C II] shell embedded in the diffuse outer shell, and both the shells seem to expand with $v_{\rm exp}$ $\sim$ 1.3 km s^{-1}. The outer shell appears to be older than the inner shell, hinting that these shells are formed sequentially. The [C II] profiles are examined toward S305, which are either double peaked or blue skewed and have the brighter redshifted component. The redshifted and blueshifted components spatially trace the inner and outer neutral shell geometry, respectively. The ionized, neutral, and molecular zones in S305 are seen adjacent to one another around the O-type stars. The regularly spaced dense molecular and dust clumps (mass $\sim$10–10^3 $M_{\odot}$) are investigated around the neutral shells, which might have originated as a result of gravitational instability in the shell of collected materials.

Unified Astronomy Thesaurus concepts: Star formation (1569); Star forming regions (1565); H II regions (694); Interstellar phases (850); Dust continuum emission (412); Interstellar emissions (840)

1. Introduction

Massive OB-type stars ($M_{*} > 8$ $M_{\odot}$) drive powerful energetics, which allow them to control the physical state of the interstellar medium (ISM). The extreme-ultraviolet (EUV; $h\nu \geqslant 13.6$ eV) photons from such massive stars ionize the hydrogen atoms and create H II regions. Due to the thermal pressure difference between the ionized region and the surrounding neutral/molecular gas, an H II region continues to grow in size and may trigger star formation in numerous ways (see the review article by Elmegreen 1998). However, the study of the interaction of massive stars with their surrounding environment is still an open research topic in astrophysics.

The surroundings of the H II regions, where the far-ultraviolet (FUV; 6 eV $\leqslant$ hν $\leqslant$ 13.6 eV) radiation plays a significant role in the heating and/or chemistry of the gas, are referred to as photodissociation regions or photon-dominated regions (PDRs; e.g., Tielens & Hollenbach 1985a, 1985b; Hollenbach & Tielens 1999). The FUV photons can dissociate the molecules and photoionize those elements having ionization potential less than the Lyman limit. The gas is primarily neutral in PDRs but still includes the tracers of singly ionized species (e.g., C^{+}, S^{+}, Si^{+}, and Fe^{+}), molecular gas (e.g., H_2 and CO), and polycyclic aromatic hydrocarbon (PAH) emission (e.g., Hollenbach & Tielens 1999; Kaufman et al. 2006). Hence, the PDRs specify the transition zone between ionized and molecular gas (see Figure 1 in Tielens & Hollenbach 1985a). Being a major coolant in PDRs, the $^2P_{3/2}$–$^2P_{1/2}$ fine-structure line of ionized carbon, [C II] 158 μm, offers a unique probe of kinematic and radiative interaction of massive stars with their surroundings (e.g., Abel et al. 2007; Schneider et al. 2020, and references therein).

In this paper, we employed the observations of the 158 μm [C II] line to study the gas dynamics of PDRs in a promising Galactic H II region, Sh 2-305 (hereafter, S305), powered by two O-type stars. In addition to the study of the spatial-kinematic structure of PDRs in S305, this paper presents the evidence of expanding [C II] shells (also abbreviated as neutral shells in this paper), hinting at the applicability of the triggered star formation scenario.

We organize this paper into six sections. Following the introduction in this section, we present an overview of the Galactic H II region S305 in Section 2. Section 3 presents the description of data sets used in this work. The observational results are presented in Section 4. The implications of our derived findings are discussed in Section 5. Finally, we summarize our major outcomes in Section 6.

2. Overview of the S305 H II Region

The S305 H II region is a part of a large molecular cloud complex located at a distance of $\sim$3.7 kpc (Pandey et al. 2020, hereafter Paper I). The molecular cloud associated with S305 has been depicted in a velocity range of [40, 48] km s^{-1} (Dewangan et al. 2020, hereafter Paper II). In Figure 1(a), we show a two-color-composite map (Spitzer 4.5 μm (red) and Spitzer 3.6 μm (green) images) of S305, displaying an extended shell-like structure. At the center of the shell-like structure, two massive O-type stars (O8.5V: VM4 and O9.5V: VM2; Vogt & Moffat 1975; Chini & Wink 1984) are located, and their positions are shown by star symbols in Figure 1(a). The positions of young stellar objects (YSOs; from Paper I) and the Giant Metrewave Radio Telescope (GMRT) 1.28 GHz

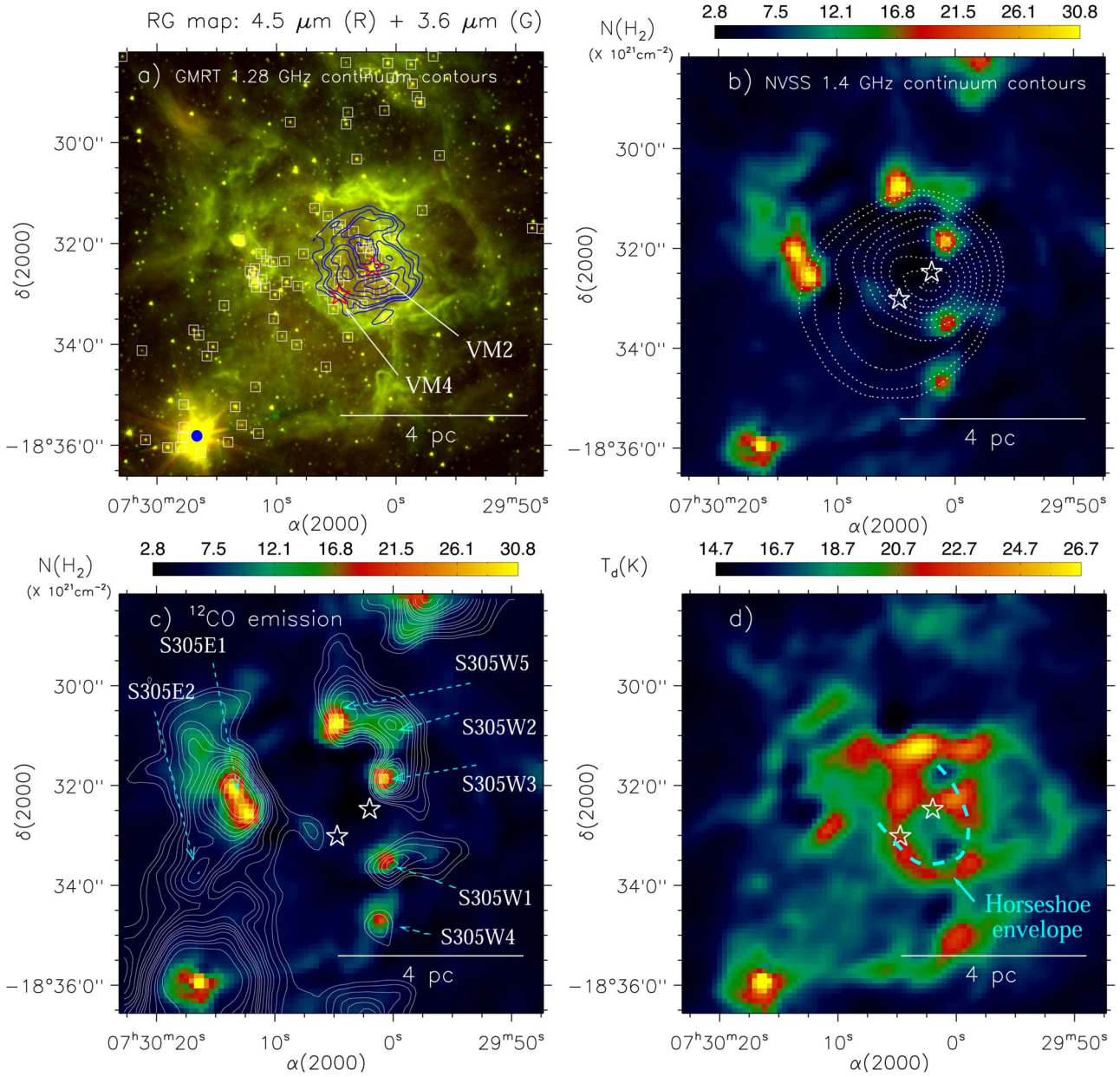

Figure 1. (a) Two-color-composite image (red: Spitzer 4.5 μm; green: Spitzer 3.6 μm) of the S305 H II region. The GMRT 1.28 GHz continuum emission contours (in blue) are overlaid with the levels of (0.4, 0.46, 0.5, 0.6, 0.7, 0.8, 0.9, 0.98) × 22 mJy beam^{-1}, where 1σ ∼ 0.74 mJy beam^{-1}. The positions of YSOs (from Pandey et al. 2020) are marked by squares. (b) Herschel column density map overlaid with the NVSS 1.4 GHz contours. The contour levels are (0.15, 0.2, 0.3, 0.4, 0.5, 0.6, 0.7, 0.8, 0.9, 0.98) × 144 mJy beam^{-1}. (c) Overlay of FUGIN ^{12}CO (1–0) emission (velocity ∼[39, 49] km s^{-1}) contours on the Herschel column density map. The contour levels are (0.2, 0.22, 0.25, 0.28, 0.3, 0.32, 0.35, 0.38, 0.4, 0.42, 0.45, 0.5, 0.53, 0.6) × 112.56 K km s^{-1}. The positions of the 850 μm continuum clumps (from Sreenilayam et al. 2014) are marked by arrows and labeled (see Figure 5 in their paper). (d) Herschel temperature map. A dashed curve (in cyan) indicates the footprint of the horseshoe envelope (see Dewangan et al. 2020, for more details). In each panel, the positions of previously known massive O-type stars are marked by star symbols and labeled in panel (a). A scale bar referring to 4 pc (at a distance of 3.7 kpc) is also displayed.

continuum contours (from Paper II) are also overlaid on the color-composite image.

In Figure 1(b), we present the Herschel column density map overlaid with the NRAO VLA Sky Survey (NVSS; resolution ∼45″; Condon et al. 1998) 1.4 GHz continuum emission contours, allowing us to infer the spatial distribution of dense condensations against the ionized gas. Figure 1(c) displays the overlay of the FUGIN[6] (resolution ∼20″; Umemoto et al. 2017) ^{12}CO (1–0) molecular emission contours on the Herschel column density map. The previously known dust clumps (from Sreenilayam et al. 2014) are also labeled in Figure 1(c). Noticeable YSOs are also found toward the dust clumps and molecular condensations, which are distributed in a regularly spaced manner around the S305 H II region. The extended structure traced in the Herschel temperature map of S305 is shown in Figure 1(d). Collectively, Figure 1 shows the multiwavelength view of S305, which was already presented and described in Papers I and II.

Previously in Papers I and II, the S305 H II region was proposed as a candidate site of triggered star formation. It was primarily investigated based on the observed morphology, the

[6] FOREST Unbiased Galactic plane Imaging survey with the Nobeyama 45-m telescope.

dynamical age of the H II region, and the fragmentation timescale of the associated molecular shell. However, a direct observational proof of the triggered star formation in S305 remains ambiguous.

3. Data Sets

3.1. SOFIA [C II] Observations

In this paper, we used the science-ready 158 μm [C II] line data cube of S305 (Project ID: 06_0226; PI: Loren Dean Anderson), which was obtained from the InfraRed Science Archive.[7] The line observations were taken with the Stratospheric Observatory for Infrared Astronomy (SOFIA)/upGREAT[8] instrument. The [C II] line data have a half-power beamwidth of 14.″1 and a velocity resolution of 0.385 km s^{-1} (see Anderson et al. 2019; Schneider et al. 2020, for data reduction procedure). We smoothed the original line data cube with a Gaussian function having a 3 pixel half-power beamwidth (i.e., 21.″15, where 1 pixel corresponds to 7.″05), which improved the image sensitivity. The resulting resolution of the line data cube is 25.″4.

3.2. Ancillary Data

We used multiscale and multiwavelength data sets, which were obtained from different existing surveys (e.g., the Warm-Spitzer GLIMPSE360 Survey ($\lambda = 3.6$ and 4.5 μm; resolution $\sim$2″; Benjamin et al. 2003; Whitney et al. 2011), the Wide-field Infrared Survey Explorer (WISE; $\lambda = 12$ μm; resolution $\sim$6.″5; Wright et al. 2010), the NVSS, and the FUGIN survey (^{12}CO/^{13}CO ($J = 1$–0); resolution $\sim$20″–21″)). Apart from these data sets, we also utilized the Herschel temperature and column density maps (resolution $\sim$12″) from Molinari et al. (2010), which were generated for the EU-funded ViaLactea project. The Bayesian PPMAP method (Marsh et al. 2015, 2017) was applied to build these Herschel maps. The GMRT radio continuum map at 1280 MHz (resolution $\sim$10″) was taken from Paper II.

4. Results

In Paper II, molecular condensations, PAH emission, dust clumps, and H_2 emission have been traced toward the horseshoe envelope surrounding the ionized shell, where noticeable YSOs are also found (see Figure 1). The ionized shell is traced by the GMRT 1.28 GHz continuum emission (see Figure 1(a)), while the footprint of the horseshoe envelope is shown by a dashed curve in Figure 1(d). In the following sections, we study new observations of the 158 μm [C II] line toward S305, enabling us to examine the spatial and velocity structure of PDRs in our target site.

4.1. The Spatial-kinematic Structure of PDRs in S305

In Figure 2(a), we show an integrated intensity (moment-0) map of the [C II] emission around S305, where the [C II] emission is integrated over a velocity range of [39.4, 49.5] km s^{-1}. The NVSS 1.4 GHz continuum emission contours are also overlaid on the [C II] emission map. The integrated [C II] emission map hints at the presence of two shell-like structures (i.e., inner and outer neutral shells) in S305. These shells can be regarded as the PDRs in the S305 region (see Section 1). The inner neutral shell, having a compact ring-like appearance, is evident with a high intensity value of [56, 110] K km s^{-1} and extends toward the eastern direction. A depreciation of the [C II] emission (i.e., a cavity), the radio continuum peak emission, and the position of the massive O9.5V star (i.e., VM2) spatially coincide and are found at the center of the inner neutral shell. The outer neutral shell is traced with the diffuse and more extended [C II] emission having a lower intensity value of [20, 55] K km s^{-1} and surrounds the inner neutral shell. The massive O8.5V star (i.e., VM4) appears to be located at the center of the outer neutral shell. This particular morphology is also seen in the Hα image from Paper II (see Figure 9 therein), which suggests that VM4 may be the major source of feedback in the dusty H II region S305. The other [C II] emission peaks are also seen toward the north and southeast directions and lie toward the locations of the previously identified clusters of YSOs (e.g., Paper I).

We show a two-color-composite map (red: [C II] moment-0 map; turquoise: WISE 12 μm image) of S305 in Figure 2(b). The spatially extended structures seem to match well in both images. In Figure 2(b), we have also marked 20 circular regions, where the gas spectra are extracted and examined. Figure 2(c) presents the [C II] moment-1 map that allows us to study the spatial distribution of the mean velocity of emitting gas. A nearly linear velocity gradient can be seen in the north–south direction. However, one can notice that the inner neutral shell is redshifted compared to the blueshifted outer/extended diffuse shell. The [C II] moment-1 map is also overlaid with the positions of previously identified ^{12}CO (2–1) molecular clumps and their velocities (Azimlu & Fich 2011; see also Paper II). The velocities of these clumps are in agreement with the velocities of the [C II] gas at corresponding positions. Nearly eight molecular clumps are found to be spatially coincident with the inner neutral shell. Six out of eight molecular clumps (i.e., c5–c10) are seen in the direction of the horseshoe envelope (see Figure 1(d)).

In order to compare the spatial structure traced by the [C II] emission and the infrared continuum images, we present the Spitzer ratio map of 4.5 μm emission to 3.6 μm emission in Figure 2(d). A detailed discussion on the ratio map is given in Paper II. The bright and dark emission zones in the ratio map detect the ionized emission and the PDR walls, respectively. One can notice from Figures 2(a) and (d) that the boundaries of the [C II] shells are well traced by the dark structures in the ratio map. Thus, the analysis of multiwavelength data confirms the presence of two shells.

Figure 3 presents the velocity channel contours of the [C II] emission overlaid on the WISE 12 μm image, enabling us to explore the gas motion. We find the spatial match of the [C II] emission with the infrared structure traced in the WISE 12 μm image. In general, the WISE 12 μm image is known to cover the prominent PAH features at 11.3 μm. In the channel maps, based on the visual inspection, we marked the boundaries of two [C II] shells by dotted circles. The larger dotted circle (center coordinates; R.A. = 07^{h}30^{m}04.^{s}51, decl. = −18°32′ 32.″72, and radius = 205″) encloses the [C II] emission of the outer diffuse shell. The outer [C II] shell is clearly seen in the velocity range from 42.1 to 44.1 km s^{-1} and has an incomplete circular (or broken ring) appearance. On the other hand, the smaller circle (center coordinates; R.A. = 07^h 30^m 02.^{s}39, decl. = −18° 32′ 19.″95, and radius = 105″) surrounds the inner [C II] shell, which is evident in the velocity channel maps from 45.2 to 47.5 km s^{-1}. In the direction of inner shell

[7] https://irsa.ipac.caltech.edu/applications/sofia

[8] upGREAT (Risacher et al. 2016) is an enhanced version of the German Receiver for Astronomy at Terahertz Frequencies (GREAT).

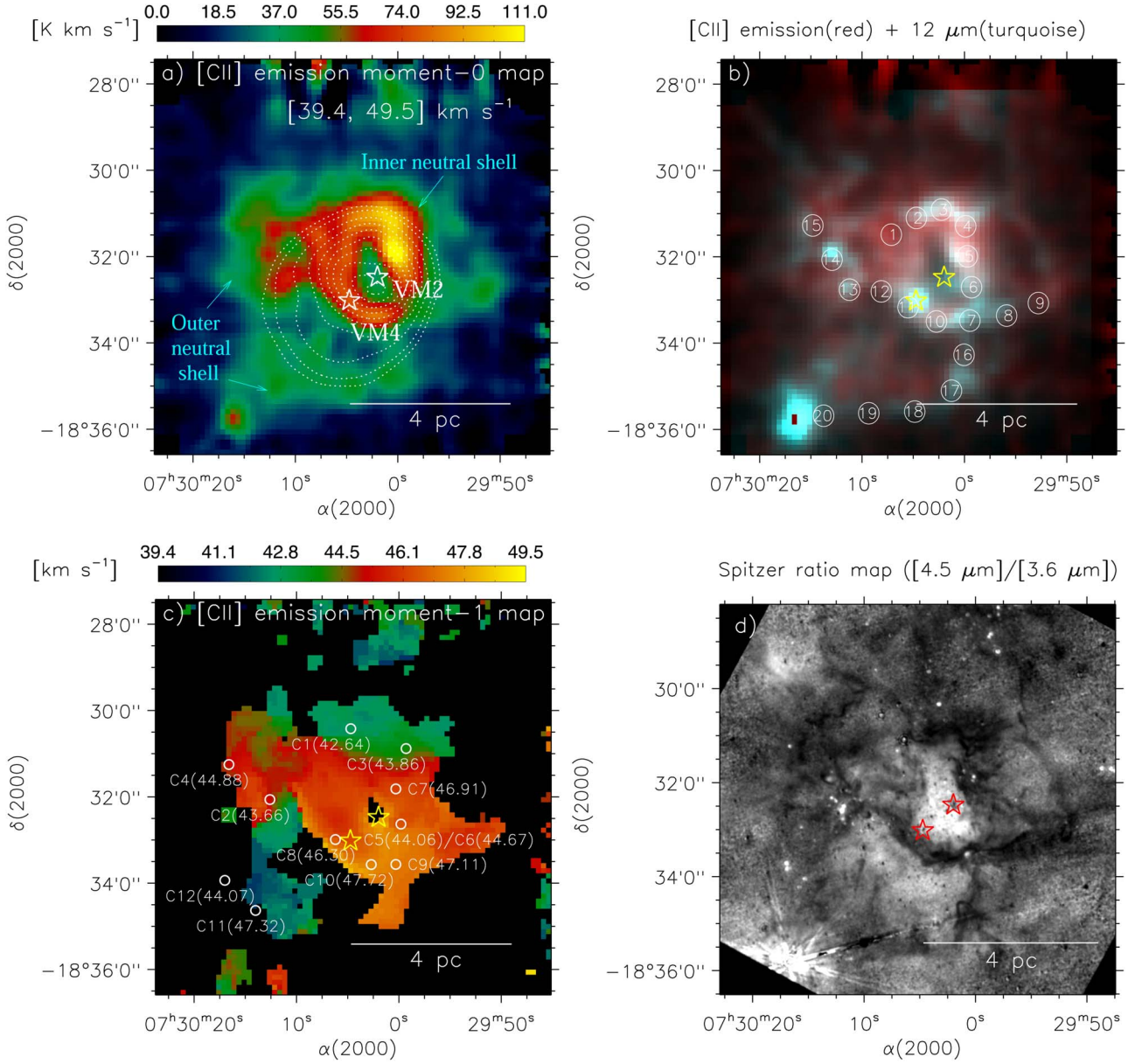

Figure 2. (a) The panel displays the [C II] integrated intensity (moment-0) map of S305. The map is overlaid with the NVSS 1.4 GHz continuum emission contours, which are the same as in Figure 1(b). (b) Two-color-composite image (red: [C II] moment-0 map; turquoise: WISE 12 μm image) of the S305 H II region. The 20 circles (radius = 15″ each) represent the areas for which the gas spectra are extracted (see Figure 4). (c) [C II] intensity-weighted mean velocity (moment-1) map overlaid with the positions of ^{12}CO (2–1) molecular clumps (from Azimlu & Fich 2011). The clumps are highlighted by open circles, and corresponding velocities are also labeled. (d) The Spitzer ratio map of 4.5 μm/3.6 μm emission (reproduced from Dewangan et al. 2020). In all the panels, the stars are the same as in Figure 1.

structure, the [C II] channel maps show that the [C II] emission is blueshifted in the northern direction, while it is strongly redshifted in the southern direction. This implies that the gas is moving toward (away from) the observer in the northern (southern) directions (e.g., Mookerjea et al. 2021). Overall, these results suggest the expansion of the gas in PDRs (see Section 5 for detailed discussion).

In order to compare the kinematics of different gas components, we have analyzed the spectral profiles of ^{12}CO/^{13}CO (1–0) and [C II] gas in Figure 4. Figure 4 displays the line profiles of the [C II], ^{12}CO (1–0), and ^{13}CO (1–0) emission toward 20 circular regions (radius = 15″ each) in the direction of S305. These regions are primarily selected toward the direction of prominent infrared features and the [C II] emission (see circles in Figure 2(b)). Each spectrum is produced by averaging the emission over the circular regions. In the direction of the compact ring feature (i.e., positions 1–15), [C II] line profiles are brighter and either are blue skewed or have double-peaked structures compared to the ^{12}CO (1–0) and ^{13}CO (1–0) profiles. The [C II] line profiles show double peaks at ∼43 and ∼47 km s^{-1} and a dip around ∼44 km s^{-1}. On the other hand, the ^{12}CO (1–0) and ^{13}CO (1–0) profiles are single peaked and lie between the double peaks of the [C II] spectra. Interestingly, all the double-peaked profiles have a brighter redshifted component than the blueshifted one (see Section 5 for more discussion).

In Figure 5, we have shown the [C II] line profiles (similar to those presented in Figure 4) with color-coded redshifted and blueshifted components. From the velocity channel maps (Figure 3), we have identified the velocity ranges of these components. The blueshifted component ([39.4, 44.4] km s^{-1}) is found to be associated with the outer shell structure, while

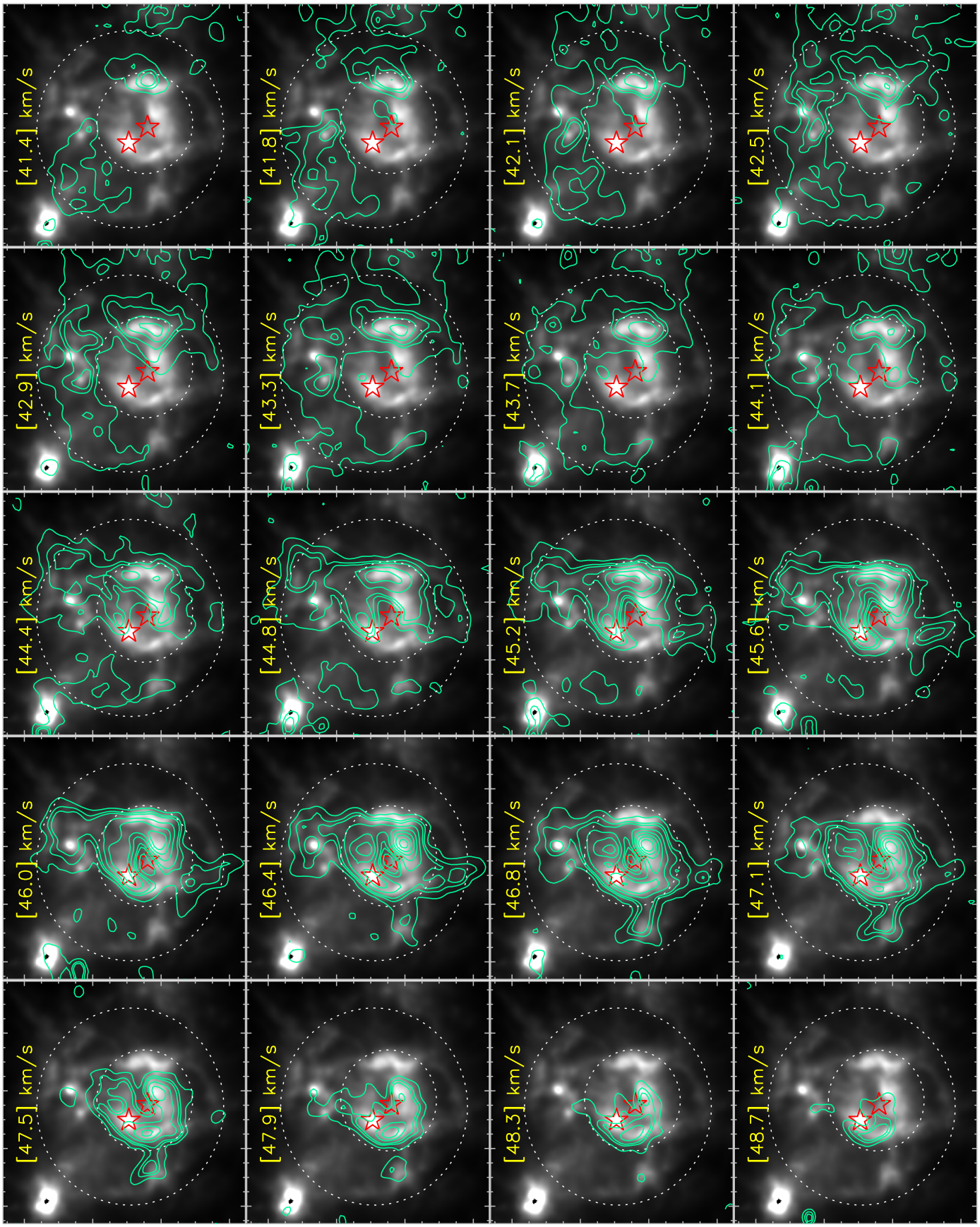

Figure 3. Velocity channel contours of the [C II] emission overlaid on the WISE 12 μm image. The velocity value is indicated in each panel (in km s^{-1}). The contours (in green) are shown with the levels of 5, 8, 10, 15, 20, 25, 30, and 35 K. The dotted circles represent the footprint of inner and outer [C II] shells. In each panel, the positions of known massive stars are marked by star symbols.

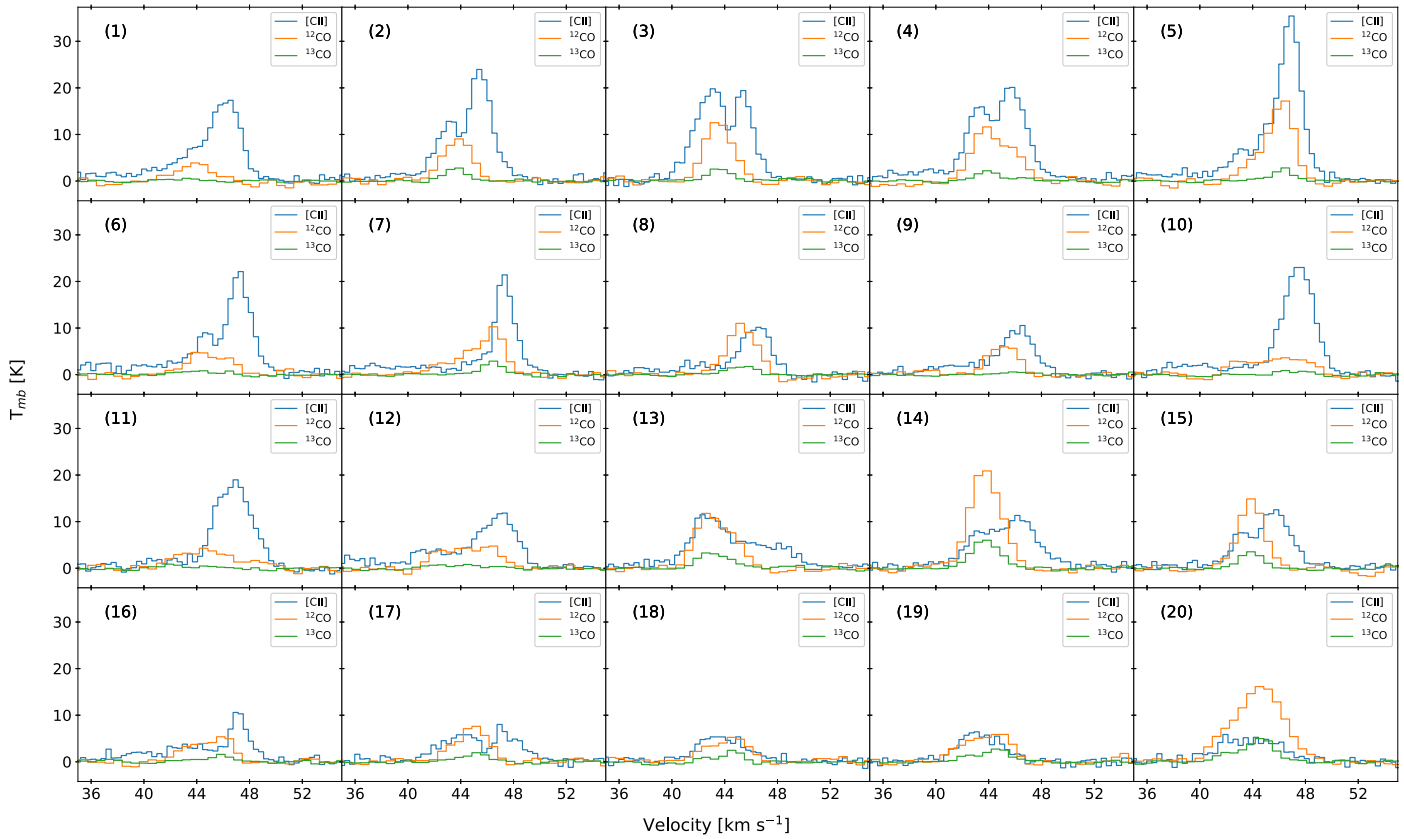

Figure 4. Profiles of the [C II], ^{12}CO (1–0), and ^{13}CO (1–0) emission toward 20 circular regions (radius = 15″ each) in S305 (see circles in Figure 2(b)). The corresponding circle number is marked in each panel.

the redshifted component ([44.4, 49.5] km s^{-1}) traces the inner shell structure. One can notice from Figure 5 that the peak of the redshifted component (i.e., 45.6 km s^{-1}; see panels 2, 3, and 4) shifts toward higher velocities as we move southward from the northern direction (see Figure 2(b)). However, the blueshifted component peaks at 43.3 km s^{-1} in all the positions and does not show much variation along the velocity axis. These results suggest the noticeable gas expansion in the inner shell compared to the outer shell. However, considering the simplistic case, we assume a similar expansion velocity for both the shells to estimate their expansion timescales (see Section 4.2).

Based on the selected velocity ranges of redshifted and blueshifted components from Figure 5, we have examined the moment maps. Figures 6(a) and (b) show the moment-0 and moment-1 maps for the redshifted component, respectively. The moment-0 map shows the inner shell structure having the compact ring-like appearance, while the moment-1 map in Figure 6(b) reveals the velocity gradient along the north–south direction of the inner shell. The velocity at the shell's rim is bluer than in the center, which favors the shell expansion. Generally, the outward displacement of the shell with increasing or decreasing velocity is referred to as the kinematic signature of an expanding shell (e.g., Pabst et al. 2019, see Figure 6 therein). Similarly, Figures 6(c) and (d) display the moment-0 and moment-1 maps for the blueshifted component, respectively. The outer shell is evident in the moment-0 map (Figure 6(c)) and has a broken ring morphology. The moment-1 map in Figure 6(d) traces the velocity field in the outer shell. A nearly linear velocity gradient is seen in the east–west direction, which may infer the direction of gas expansion in the outer shell. However, the velocity structure is more complex in the outer shell than the inner shell, which makes it more difficult to interpret.

In order to compare the spatial distribution of different components of gas (i.e., ionized, neutral, and molecular) in S305, we show a three-color (red: GMRT 1.28 GHz; green: FUGIN ^{12}CO (1–0); blue: SOFIA [C II] 158 μm) composite image in Figure 7(a). All three components of gas are clearly distinguishable. In the direction of the observed [C II] emission, the molecular CO is less abundant or mostly absent (see also Figure 4). The distribution of the molecular gas is clumpy rather than a diffuse appearance. Figure 7(b) displays the [C II] emission contours for the inner and outer shell structures (see Figures 6(a) and (c)). The detailed interpretation of the shell structures is discussed in Section 5.1.

To study the spatial-kinematic structures of the PDRs in S305, we have studied the position–velocity (PV) diagrams of different gas components. Figures 8(a) and (b) show the PV diagrams of [C II], ^{12}CO (1–0), and ^{13}CO (1–0) emission in two different directions, i.e., perpendicular to and along the line joining the stars VM2 and VM4, respectively. The positive offsets in the positions are measured along the southwest and northwest directions for the two PV diagrams. We have overlaid the emission contours of ^{13}CO (1–0) (in red) and [C II] (in violet) on the ^{12}CO (1–0) PV emission map, allowing us to study the spatial-kinematic structures of different components of gas. The 1.28 GHz radio brightness profile is also shown in each panel, specifying the position of the H II region. The detailed outcomes from this analysis are discussed in Section 5.

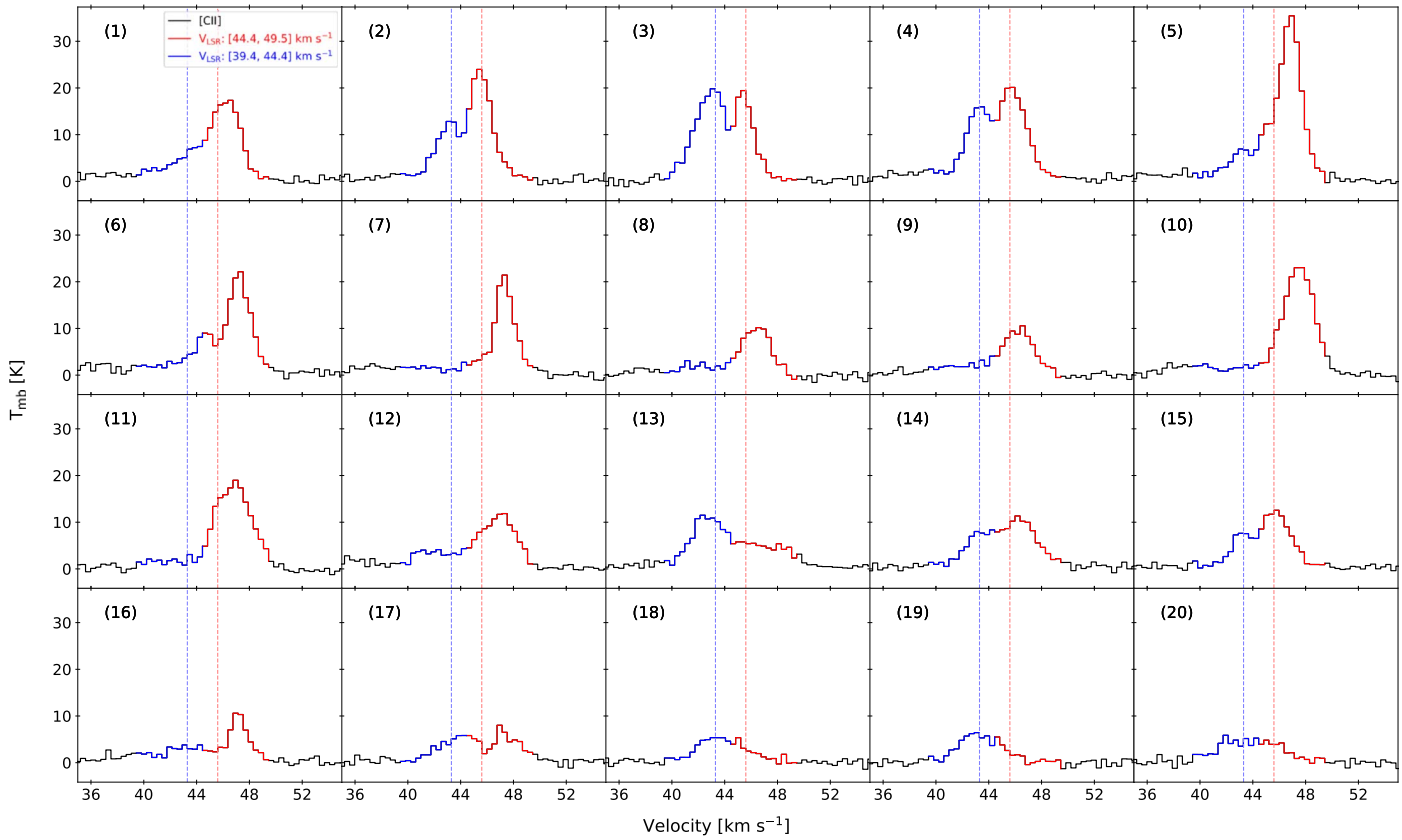

Figure 5. Profiles of the [C II] emission, similar to those shown in Figure 4. The blue and red components in the [C II] profiles correspond to the velocity range of [39.4, 44.4] km s^{-1} and [44.4, 49.5] km s^{-1}, respectively. These velocity ranges are used to disentangle the inner and outer [C II] shells (see Section 4.1 for more details). The vertical dashed lines in blue and red represent the velocities of 43.3 and 45.6 km s^{-1}, respectively.

4.2. Physical Parameters of the [C II] Shells

We have estimated the neutral hydrogen column density (N(H)) and the mass of the [C II]-emitting gas toward the compact and the extended feature (i.e., inner and outer neutral shells). The column density depends on the luminosity ratio of the [C II] line in the PDR to that of the H II region as follows (see Equation A4 in Kaufman et al. 2006):

$$N(\mathrm{H}) = \left(\frac{L_{\mathrm{CII}}(\mathrm{PDR})}{L_{\mathrm{CII}}(\mathrm{HII})}\right)\frac{Z n_e^{1/3}\Phi_{49}^{1/3} f_{\mathrm{C}^+}}{15} \times 10^{21}\ (\mathrm{cm}^{-2}), \quad (1)$$

where $\Phi_i = 10^{49}\Phi_{49}$ s^{-1} is the absolute luminosity of ionizing EUV photons, f_{C^+} is the fraction of singly ionized carbon, $Z = 1$ relates to the standard abundance or metallicity, and n_e is the number density of electrons. From the [C II] integrated intensity map, we have estimated the value of $\frac{L_{\mathrm{CII}}(\mathrm{PDR})}{L_{\mathrm{CII}}(\mathrm{HII})}$ around 9. In this exercise, we consider that the [C II] emission, which spatially overlaps with the 1.28 GHz continuum emission (i.e., H II region), belongs to the H II region and the rest of the emission corresponds to the part of PDRs.

For the typical values of $Z = 1$, $n_e = 500$ cm^{-3}, $\Phi_i = 10^{49}$ s^{-1}, and $f_{\mathrm{C}^+} = 0.1$ (adopted from Kaufman et al. 2006; Kirsanova et al. 2020), the derived N(H) and the total mass of the [C II]-emitting gas in the PDRs are $\sim 5 \times 10^{20}$ cm^{-2} and $\sim$565 $M_\odot$, respectively. The mass calculation is based on the assumption that PDRs have the shape of layers on the sphere, and all the material is in the form of neutral hydrogen. We calculated the layer widths from the PV diagrams (Figure 8). To compute the total mass of the shells, we used the mass −column density relation of $M_{\mathrm{shell}} = m_{\mathrm{H}}\, a_{\mathrm{shell}}\, \Sigma N(\mathrm{H})$, where a_{shell} is the shell area, m_{H} is the mass of hydrogen atom, and ΣN(H) is the integrated column density over the shell area. In this exercise, the uncertainty caused by the noise is around 10%, but the assumptions of different parameters (e.g., n_e, f_{C^+}, and Φ_i from Kaufman et al. 2006; Kirsanova et al. 2020) can change the outcomes accordingly. The hydrogen column density (or shell mass) can also be derived from the [C II] emission, which first requires the estimation of [C II] column density (N([C II])). Since the optically thin [^{13}C II] line is not detected in present observations, we can assume [C II] emission as optically thin and then compute N([C II]) using Equation (4) in Kirsanova et al. (2020). Assuming a typical excitation temperature of $T_{\mathrm{ex}} = 120$ K, the observed average N([C II]) is $\sim 4 \times 10^{17}$ cm^{-2}. Now, using the gas-phase carbon abundance of [C/H] $= 1.6 \times 10^{-4}$ (Sofia et al. 2004), we evaluated the N(H) as $\sim 2 \times 10^{21}$ cm^{-2}, which is almost close to the previously calculated N(H) value of $\sim 5 \times 10^{20}$ cm^{-2}.

We have also estimated the expansion timescale of each [C II] shell, considering that the expansion is caused by a continuous flow of stellar winds (e.g., Castor et al. 1975; Weaver et al. 1977). The radii (R_{s}) of the inner and outer shells are computed from the PV diagrams and the velocity channel maps (see dotted circles in Figure 3) and are $\sim$1.9 and $\sim$3.7 pc, respectively. We have evaluated the expansion velocity of $v_{\mathrm{exp}} \sim 1.3$ km s^{-1}, assuming that the shells expand in both directions (e.g., Pabst et al. 2020, see Section 3.2.2 and Appendix B therein). Here, we also note that the expansion

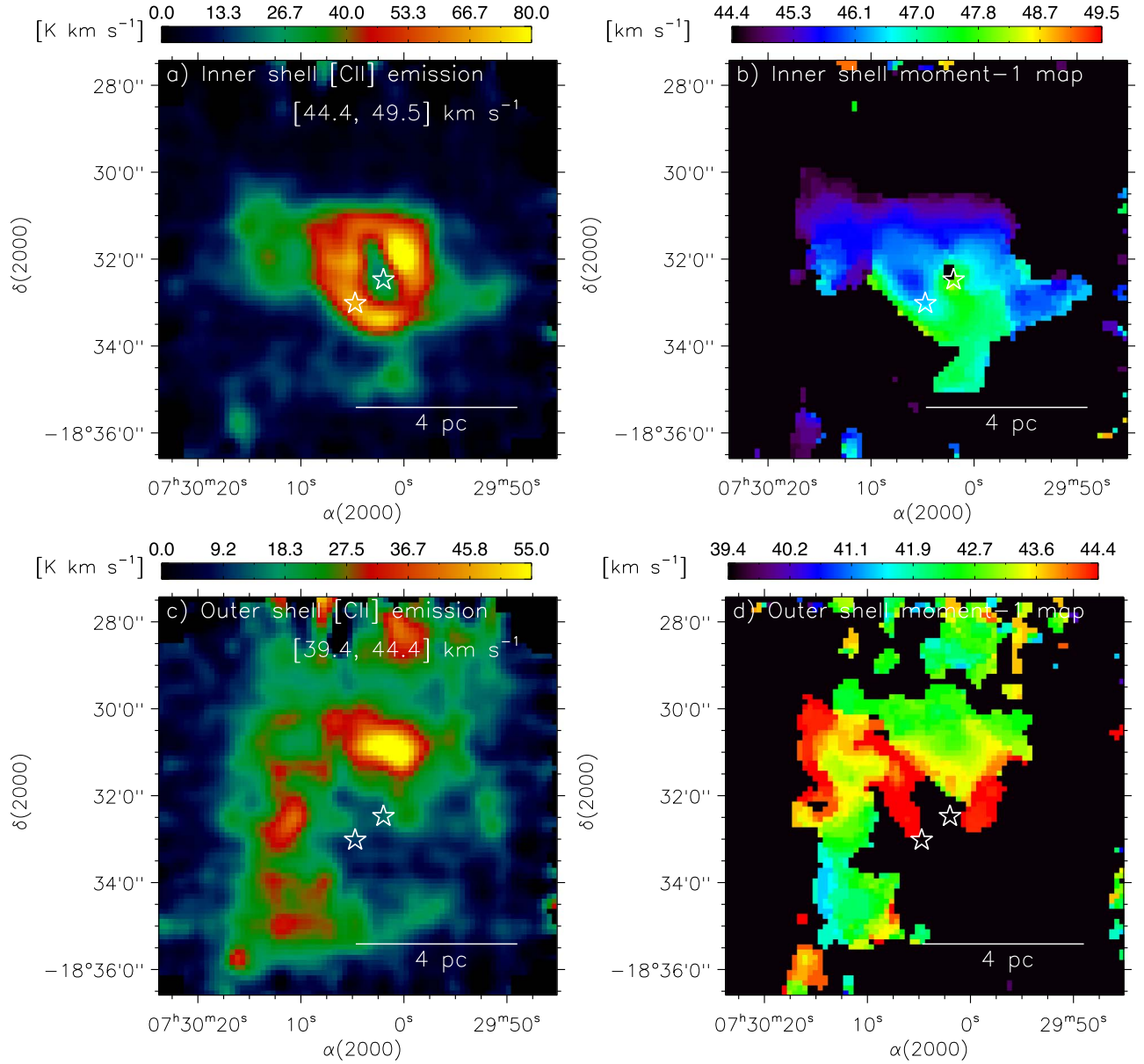

Figure 6. Top panels display (a) moment-0 map and (b) moment-1 map of the [C II] emission in the velocity range of [44.4, 49.5] km s^{-1} (see red component of the [C II] profiles in Figure 5). Bottom panels show the same maps as in the top panels, but for the outer [C II] shell (see blue component of the [C II] profiles in Figure 5). In all the panels, the stars are the same as in Figure 1.

velocity can range from 1 to 4 km s^{-1} (see PV diagrams in Figure 8), and for calculation purposes, we have used our calculated value of ∼1.3 km s^{-1}. Considering a similar expansion velocity of $v_{\rm exp}$ ∼ 1.3 km s^{-1} for both the shells, the expansion timescales of the inner and outer shells are determined to be ∼0.9 and ∼1.7 Myr, respectively. To compute the expansion timescale, we used the following equation (e.g., Weaver et al. 1977; Pabst et al. 2020):

$$t_{\rm exp} \simeq 0.6\left(\frac{R_{\rm s}}{1\ {\rm pc}}\right)\left(\frac{1\ {\rm km\ s^{-1}}}{v_{\rm exp}}\right){\rm Myr}. \quad (2)$$

Here, one can note that the systematic uncertainties in the estimation of shell extent, the expansion velocity, and the expansion timescale are about 30%–50%.

5. Discussion

In this paper, for the first time, we examined the structure and gas dynamics of PDRs in S305 using the neutral gas tracer, 158 μm [C II] line. The neutral gas is traced in the velocity range of [39.4, 49.5] km s^{-1}, which is consistent in velocity with the molecular gas (see Figure 4 and Paper II). The ionized, neutral, and molecular gas are spatially distributed in the hierarchy manner (i.e., adjacent to one another; see Figure 7(a)) in S305, which agrees well with the one-dimensional models of PDRs (e.g., Tielens & Hollenbach 1985a, see Figure 1 therein). In Figure 7(a), the boundary, traced by the [C II] gas, is well distinct from that of ionized gas and molecular CO. This is probably possible because the CO molecules, in the direction of massive stars and our line of sight, are mostly dissociated and the carbon is ionized, which contributes to the [C II] emission

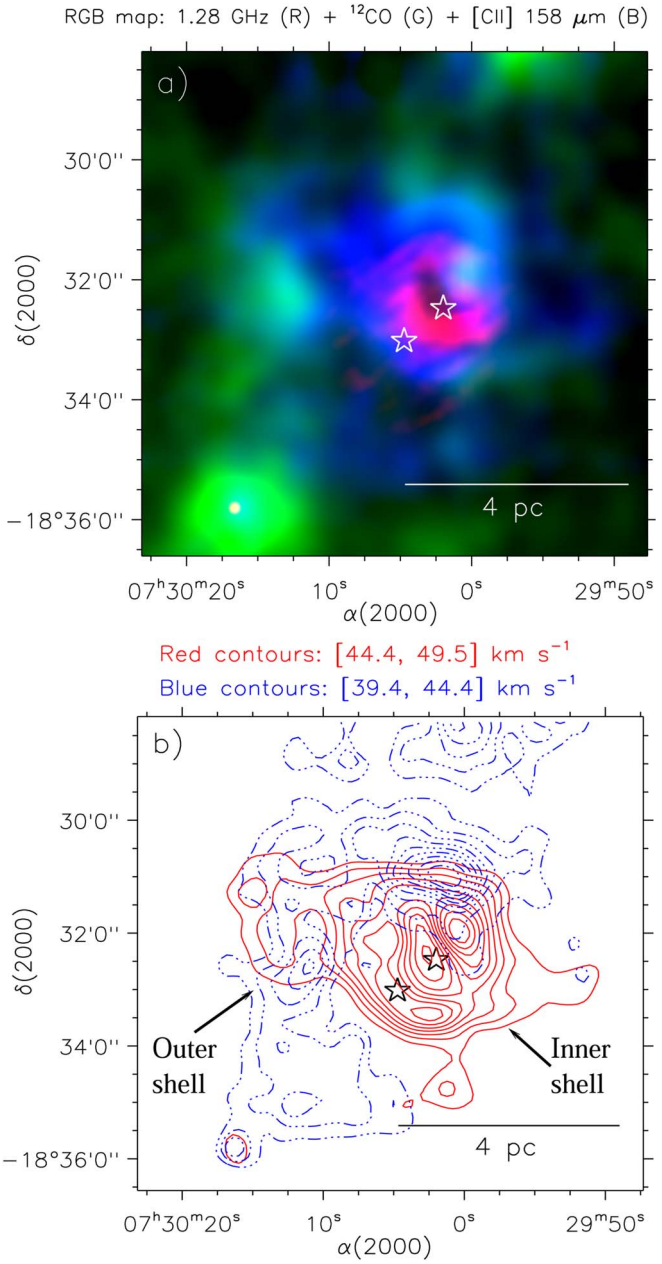

Figure 7. (a) Three-color (red: GMRT 1.28 GHz; green: FUGIN ^{12}CO (1–0); blue: SOFIA [C II] 158 μm) composite map of S305. (b) The [C II] emission contours for the inner (in red) and outer (in blue) shell structures. The red contour levels range from 23.34 to 93.36 K km s^{-1} in steps of 7.78 K km s^{-1}, while the blue contour levels range from 19.57 to 65.24 K km s^{-1} in steps of 5.07 K km s^{-1}. The stars are the same as in Figure 1.

in PDRs around S305. It seems that the [C II] emission traces the unshielded H_2 gas in PDRs, where molecular gas tracer CO is photodissociated.

5.1. Double [C II] Shells in PDRs around S305

The two [C II] shells in S305 are evident from the channel maps shown in Figure 3. The outer shell has a more extended diffuse structure and unveils its broken morphology, while the inner shell reveals a compact ring-like feature (see Section 4.1 and Figure 6). Recently, Kirsanova et al. (2020) performed the spherically symmetric chemodynamical model of expanding H II regions in the site S235. The PV diagrams shown in Figure 8 are close to the numerical model by Kirsanova et al. (2020). In the direction of the line joining stars VM2 and VM4, the shape of the PV diagram is somewhat symmetrical for the individual shells and has a typical double-peaked structure (i.e., similar to the dumbbell shape; see Figure 8(b)). The footprint of the diffuse shell can be seen in the positive and negative offsets ([C II] contour of 3 K), while the compact shell is seen toward the positive offset ([C II] contours of 6–30 K) only. The velocity of the extended diffuse shell is around ∼44 km s^{-1}, compared to the compact shell having a velocity of ∼46.5 km s^{-1}. The molecular gas walls are formed around the diffuse shell as seen in ^{12}CO (1–0) and ^{13}CO (1–0) peaks at ∼44 km s^{-1}.

The PV diagram (Figure 8(b)) also infers the geometric distribution of the two [C II] shells. In the direction of the compact shell, the molecular gas wall, which is kinematically related to the diffuse shell wall, shows a peak emission at ∼46 km s^{-1}. This molecular peak emission exactly matches with one of the two [C II] peaks (located at 1.′7 offset and ∼46 km s^{-1}). The other [C II] peak related to the compact shell (located at 0′ offset and ∼46 km s^{-1}) in the PV diagram is situated in the center of the diffuse shell. The absence of the molecular wall in this peak suggests that the compact zone is embedded into the extended diffuse shell. This particular observation provides the only evidence of geometrically inner (compact shell) and outer (diffuse shell) morphology of the [C II]-emitting gas. The PV structures in the different directions are far from symmetry, as shown in the PV diagram in the perpendicular direction of the line joining stars VM2 and VM4 (see Figure 8(a)). Such asymmetry can arise from the inhomogeneity of the surrounding gas. These kinematical structures may be explained by the triggered formation scenario of the compact zone, where the parental gas is compressed by the expansion of the diffuse shell. The H II zone lies at the center of the diffuse shell as shown by the 1.28 GHz continuum emission profile and is the outcome of EUV flux from the stars VM2 and VM4 (Paper II). The gas is being pushed to the observer, leading to the Doppler shift of the [C II] emission. The compact H II zone expands to the inner regions of the diffuse shell, which can explain the asymmetry in the PV diagrams. The gas expansion in the inner [C II] shell is clearly evident from the velocity channel maps (Figure 3) and moment-1 map (Figure 6(b)). However, it is not very significant in the case of the outer shell, which, however, shows the southeast-to-southwest velocity gradient (see Figure 6(d)).

The shells are not kinematically homogeneous but are close to the expanding bubbles. In Section 4.2, the expansion timescales of the inner and outer shells are determined to be ∼0.9 and ∼1.7 Myr, respectively. The expansion timescales of the shells agree with the dynamical age of the S305 H II region (i.e., ∼0.5–1.7 Myr; Paper II) and with the average age of the stellar population in S305 (i.e., ∼1.8 Myr; Paper I). These results infer that the inner shell is younger than the outer shell, suggesting that the shells have formed sequentially. It may be possible that the star VM4 played a major role in the formation of the outer shell, while the inner shell formation seems to be linked to the star VM2 (see also Figures 2 and 3). Furthermore, based on the morphology and kinematics of the [C II] shells, we cannot rule out the possibility of the influence of the star VM4 in the formation of the star VM2. However, it requires the

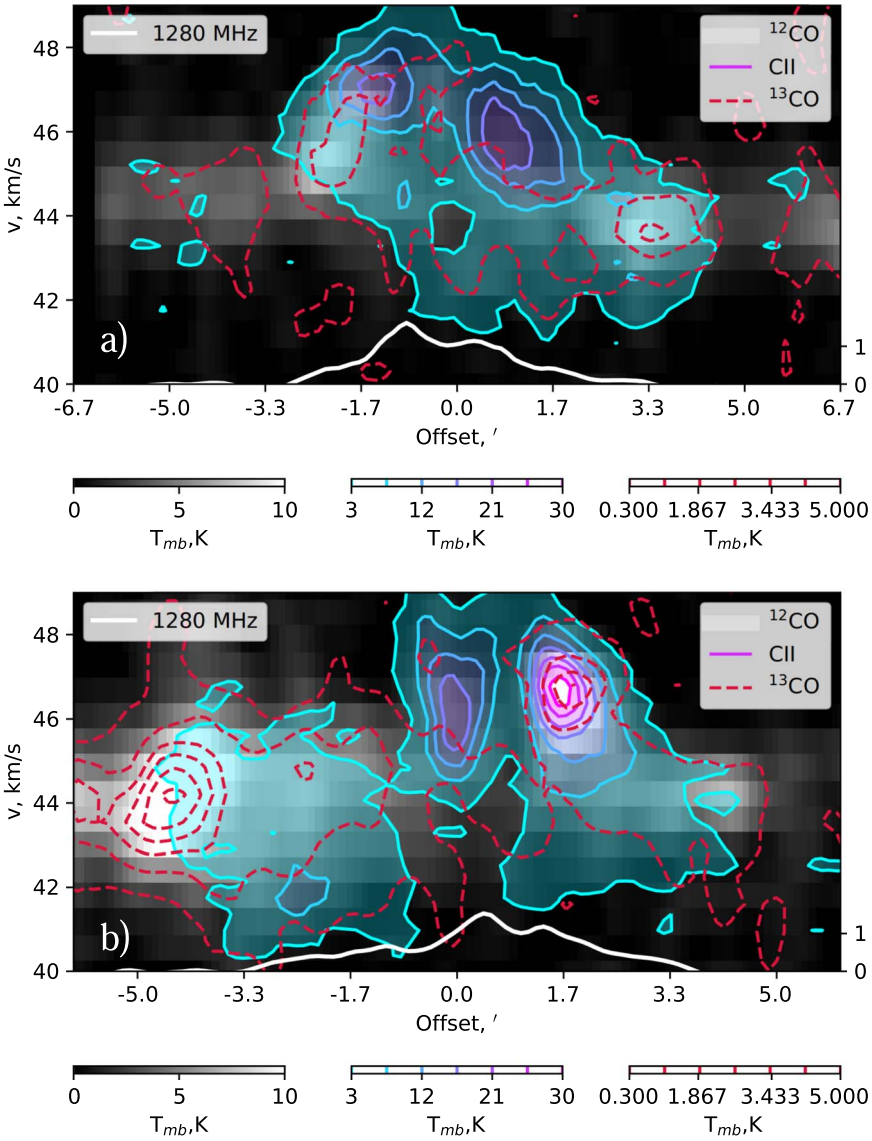

Figure 8. PV diagrams of the ^{12}CO (1–0) (gray emission), ^{13}CO (1–0) (dashed contours), and [C II] (thick contours) emission: (a) perpendicular to the line joining VM2 and VM4; (b) along the line joining VM2 and VM4. The corresponding color bars are shown below the panels. In each panel, the 1280 MHz radio continuum emission profile (a thick white curve) is also shown, which is multiplied by a factor of 100. The radio continuum brightness scale bar is shown to the right in each panel and has units of mJy beam^{-1}.

proper age estimation of these stars, which is beyond the scope of this paper.

In the direction of S305, we find the double-peaked line profiles of the [C II] emission compared to the single-peaked line profiles of ^{12}CO (1–0) and ^{13}CO (1–0) (see Figure 4). From the analysis of the [C II] spectra taken at different positions in S305 (Figure 5), we found that the blueshifted and redshifted components spatially trace the outer and inner shell morphology, respectively (see Figure 6). It is quite interesting to note that the outer shell, which is more diffuse compared to the inner shell, lies in front of the inner shell. We note that the double-peaked [C II] profiles are dominant in the northern high-intensity zone of the inner neutral shell (see Figures 2(b) and 5), which are spatially seen in the direction of overlapping areas of the inner and outer [C II] shells (see also Figure 7(b)). It has been shown in the previous studies that the presence of an enhanced redshifted peak in the significant optically thick lines is the signature of the expansion scenario (e.g., Pavlyuchenkov et al. 2008). In S305, the majority of the [C II] profiles (Figure 4) are either double peaked (with brighter redshifted component) or blue skewed, suggesting the gas expansion in PDRs, which is further confirmed by the [C II] channel maps and the PV diagrams.

5.2. Star Formation Scenario in S305

In the literature, it has been a common practice to use the mid-infrared images as a tool for qualitative identification of bubble structures or triggered star formation sites (e.g., Deharveng et al. 2005, 2010; Zavagno et al. 2006, 2007). Different scenarios of triggered/sequential star formation are available in the literature (e.g., Elmegreen 1998). The expansion of an H II region may initiate the instability in preexisting dense regions of gas (i.e., "radiation-driven implosion" scenario; Bertoldi 1989; Lefloch & Lazareff 1994) or may accumulate the layers of dust and gas between the ionization and shock fronts that later become gravitationally unstable and form next-generation stars (i.e., "collect and

collapse" scenario; Elmegreen & Lada 1977; Whitworth et al. 1994). Despite the enumerable wealth of literature in theoretical works, the direct observational evidence of "triggered/sequential star formation" is still lacking (e.g., Deharveng et al. 2010; Dale et al. 2015, and references therein).

In the mid-infrared images, the 24 μm emission correlates to the ionized zone, while the 8 μm emission traces the boundary of dust condensation and the ionization front. The shock front can be traced by H_2 emission. In S305, the H_2 emission is prominently found in the direction of the horseshoe envelope (see Figure 3 in Paper II). The presence of regularly spaced massive fragments in the periphery or along the direction of PDRs is evident in the dust emission at 850 μm (see Figure 1(c)) and in the form of molecular clumps (see Figure 2(c)). These clumps are spatially seen in the direction and/or the boundary of the [C II] shells, which are also kinematically related to the [C II]-emitting gas. The masses of dust and molecular clumps are in the range of $M_{\rm clumps}^{850\,\mu{\rm m}}$ $\sim$10–10^3 $M_\odot$ (see Table 6 in Sreenilayam et al. 2014) and $M_{\rm clumps}^{\rm CO(2-1)}$ $\sim10^2$–10^3 $M_\odot$ (see Table 3 in Azimlu & Fich 2011), respectively. Apart from this, Paper I identified the massive dense clumps/fragments using the Herschel column density map. These clumps have size extensions in parsecs (i.e., radii $\sim$0.28–1.32 pc), and their masses range from 35 to 1565 $M_\odot$. Hence, it is possible that during the expansion of an H II region the dense materials have been collected between the ionization and shock fronts, which now appear in the form of dense fragments.

Therefore, all the outcomes together confirm the gas expansion in PDRs followed by the collection of materials (e.g., dust and gas) around it. The presence of massive neutral shells, dust, and gas clumps around H II region S305 strengthens the applicability of the "collect and collapse" scenario as suggested in Paper II.

6. Summary and Conclusion

The present paper analyzes the unpublished 158 μm [C II] line data, which enables us to study the kinematics of gas in PDRs around the H II region S305 hosting two massive O-type stars (i.e., VM2 and VM4). Using the [C II] line data, the neutral gas in PDRs is examined in a velocity range of [39.4, 49.5] km s^{-1}. Two shell-like structures (i.e., inner: an intense ring-like shell; outer: the extended and diffuse neutral shell) are found in the [C II] moment-0 map and velocity channel maps. In the direction of S305, the [C II] line profiles are double peaked (with enhanced redshifted component), peaking at $\sim$43 and $\sim$47 km s^{-1} and showing a dip at $\sim$44 km s^{-1}. The dip in double-peaked [C II] profiles coincides with the peaks of ^{12}CO/^{13}CO (1–0) line profiles. The double-peaked [C II] spectra spatially trace two shells in PDRs around S305. The PV diagrams confirm that the compact shell is geometrically embedded in the outer diffuse shell, and both the shells are enclosed by the molecular gas walls. Based on the [C II] emission, the estimated average neutral hydrogen column density and the mass of the [C II] shells are $\sim5\times10^{20}$ cm^{-2} and $\sim$565 $M_\odot$, respectively. The PV diagrams, including the spectral profiles and velocity channel maps, unveil the signatures of gas expansion in PDRs. The expansion velocity of $v_{\rm exp}\sim$ 1.3 km s^{-1} implies the expansion timescales of $\sim$0.9 and $\sim$1.7 Myr for the inner and outer shells, respectively. This suggests that the two [C II] shells are formed sequentially in S305. The consistent velocity and spatial structures of regularly spaced massive dust and molecular fragments to those of the neutral gas/PDRs confirm that these fragments are the outcome of the gravitational collapse of a shell of collected materials.

We thank the anonymous reviewer for valuable comments that have improved the scientific quality of the paper. The research work at Physical Research Laboratory is funded by the Department of Space, Government of India. D.K.O. acknowledges the support of the Department of Atomic Energy, Government of India, under Project Identification No. RTI 4002. I.I.Z. and P.M.Z. acknowledge the support of the Russian Science Foundation (grant No. 17-12-01256). This work is based on observations made with the NASA/DLR Stratospheric Observatory for Infrared Astronomy (SOFIA). SOFIA is jointly operated by the Universities Space Research Association, Inc. (USRA), under NASA contract NAS2-97001, and the Deutsches SOFIA Institut (DSI) under DLR contract 50 OK 0901 to the University of Stuttgart. This work is based (in part) on observations made with the Spitzer Space Telescope, which is operated by the Jet Propulsion Laboratory, California Institute of Technology, under a contract with NASA. This publication makes use of data from FUGIN, FOREST Unbiased Galactic plane Imaging survey with the Nobeyama 45 m telescope, a legacy project in the Nobeyama 45 m radio telescope.

ORCID iDs

N. K. Bhadari https://orcid.org/0000-0001-8812-8460
L. K. Dewangan https://orcid.org/0000-0001-6725-0483
P. M. Zemlyanukha https://orcid.org/0000-0003-4999-1741
D. K. Ojha https://orcid.org/0000-0001-9312-3816
I. I. Zinchenko https://orcid.org/0000-0003-2793-8229
Saurabh Sharma https://orcid.org/0000-0001-5731-3057

References

Abel, N. P., Sarma, A. P., Troland, T. H., et al. 2007, ApJ, 662, 1024
Anderson, L. D., Makai, Z., Luisi, M., et al. 2019, ApJ, 882, 11
Azimlu, M., & Fich, M. 2011, AJ, 141, 43
Benjamin, R. A., Churchwell, E., Babler, B. L., et al. 2003, PASP, 115, 953
Bertoldi, F. 1989, ApJ, 346, 735
Castor, J., McCray, R., & Weaver, R. 1975, ApJL, 200, L107
Chini, R., & Wink, J. E. 1984, A&A, 139, L5
Condon, J. J., Cotton, W. D., Greisen, E. W., et al. 1998, AJ, 115, 1693
Dale, J. E., Haworth, T. J., & Bressert, E. 2015, MNRAS, 450, 1199
Deharveng, L., Schuller, F., Anderson, L. D., et al. 2010, A&A, 523, 6
Deharveng, L., Zavagno, A., & Caplan, J. 2005, A&A, 433, 565
Dewangan, L. K., Sharma, S., Pandey, R., et al. 2020, ApJ, 898, 172
Elmegreen, B. G. 1998, ASPC, 148, 150
Elmegreen, B. G., & Lada, C. J. 1977, ApJ, 214, 725
Hollenbach, D. J., & Tielens, A. G. G. M. 1999, RvMP, 71, 173
Kaufman, M. J., Wolfire, M. G., & Hollenbach, D. J. 2006, ApJ, 644, 283
Kirsanova, M. S., Ossenkopf-Okada, V., Anderson, L. D., et al. 2020, MNRAS, 497, 2651
Lefloch, B., & Lazareff, B. 1994, A&A, 289, 559
Marsh, K. A., Whitworth, A. P., & Lomax, O. 2015, MNRAS, 454, 4282
Marsh, K. A., Whitworth, A. P., Lomax, O., et al. 2017, MNRAS, 471, 2730
Molinari, S., Swinyard, B., Bally, J., et al. 2010, PASP, 122, 314
Mookerjea, B., Sandell, G., Veena, V. S., et al. 2021, A&A, 648, A40
Pabst, C., Higgins, R., Goicoechea, J. R., et al. 2019, Natur, 565, 618
Pabst, C. H. M., Goicoechea, J. R., Teyssier, D., et al. 2020, A&A, 639, A2
Pandey, R., Sharma, S., Panwar, N., et al. 2020, ApJ, 891, 81
Pavlyuchenkov, Y., Wiebe, D., Shustov, B., et al. 2008, ApJ, 689, 335
Risacher, C., Güsten, R., Stutzki, J., et al. 2016, A&A, 595, A34
Schneider, N., Simon, R., Guevara, C., et al. 2020, PASP, 132, 104301
Sofia, U., Lauroesch, J., Meyer, D., & Cartledge, S. 2004, ApJ, 605, 272
Sreenilayam, G., Fich, M., Ade, P., et al. 2014, AJ, 147, 3
Tielens, A. G. G. M., & Hollenbach, D. 1985a, ApJ, 291, 722
Tielens, A. G. G. M., & Hollenbach, D. 1985b, ApJ, 291, 747

Umemoto, T., Minamidani, T., Kuno, N., et al. 2017, PASJ, 69, 78
Vogt, N., & Moffat, A. F. J. 1975, A&A, 45, 405
Weaver, R., McCray, R., Castor, J., Shapiro, P., & Moore, R. 1977, ApJ, 218, 377
Whitney, B., Benjamin, R., Meade, M., et al. 2011, BAAS, 43, 241.16
Whitworth, A. P., Bhattal, A. S., Chapman, S. J., et al. 1994, MNRAS, 268, 291
Wright, E. L., Eisenhardt, P. R. M., Mainzer, A. K., et al. 2010, AJ, 140, 1868
Zavagno, A., Deharveng, L., Comerón, F., et al. 2006, A&A, 446, 171
Zavagno, A., Pomarès, M., Deharveng, L., et al. 2007, A&A, 472, 835